This is the accepted manuscript made available via CHORUS. The article has been published as:

Universality and microstrain origin of the ramp reversal memory effect

Elihu Anouchi, Naor Vardi, Yoav Kalcheim, Ivan K. Schuller, and Amos Sharoni

Phys. Rev. B **106**, 205145 — Published 28 November 2022

DOI: 10.1103/PhysRevB.106.205145

Universality and Micro-Strain Origin of the Ramp Reversal Memory Effect

*Elihu Anouchi[1], Naor Vardi[1], Yoav Kalcheim[2,3], Ivan K. Schuller[2] and Amos Sharoni[1,]**

[1]Department of Physics & Institute of Nanotechnology and Advanced Materials, Bar Ilan University, Ramat-Gan, 590002, Israel.

[2]Department of Physics, University of California San Diego, La Jolla, CA 92093, USA

[3]Department of Materials Science and Engineering, Technion, Israel Institute of Technology, Haifa, 3200003, Israel

*Corresponding author: amos.sharoni@biu.ac.il

Keywords: Ramp reversal memory, insulator-metal transition, transition metal oxides, vanadium oxide, strain engineering.

ABSTRACT

The recently discovered ramp reversal memory (RRM) [Adv. Mater. 2017, **29**, 1605029] is a non-volatile memory effect observed in correlated oxides with temperature-driven insulator-metal transitions (IMT). It appears as a resistance increase at predefined temperatures that are set or erased by simple heating-cooling (i.e., ramp-reversal) protocols. Until now RRM was measured for two materials - VO_2 and $NdNiO_3$. A heuristic model suggests that the RRM is caused by a local transition temperature increase at boundaries of spatially separated metallic and insulating domains during ramp-reversal. However, there is no experimental measure of the magnitude of the effect, which is crucial for the development of a theoretical account of the RRM.

Here we show that V_2O_3 also shows RRM including all related features, highlighting the generality of the effect. Moreover, an analysis of the RRM as an effective (average) increase of the critical temperature provides a quantitative measure of its magnitude as a function of temperature and ramp-reversal protocols. We provide clear evidence that the RRM is the outcome of local increase in T_c of the microscopic-scale phase-boundaries, which are created during temperature ramp-reversal (from heating to cooling) within the insulator-metal phase coexistence regime.

Electronic phase transition in correlated oxides is generally associated with the existence of competing ground states and coupling between different degrees of freedom, including spins, lattice strains, orbitals and phonons, that have similar energy scales. [1–4] The complex nature of these correlated electron systems opens the possibility for modifying the ground state by a variety of driving forces, and for phase transitions and other unexpected phenomena to appear [1,5–7]. We have recently reported an unexpected memory effect – the ramp reversal memory (RRM), [8] observed as a resistance change during the insulator-metal transition (IMT).

The RRM was observed to date in only two correlated transition metal oxides – VO_2 and $NdNiO_3$ thin films, which have a temperature driven insulator-metal transition (IMT) coinciding with a structural transition. [9,10] The RRM is observed in resistance vs. temperature (R vs. T) measurements of the phase transition, and is induced by applying simple heating and cooling protocols. The sample is initially cooled from the fully metallic to the fully insulating state. Then it is heated to a chosen "reversal temperature" - T_R, within the metal-insulator phase coexistence regime. [11,12] Thereafter, the sample is cooled back to the insulating state. After the reversal loop, the resistance of the sample is measured while heating from the insulating to the metallic state. As a consequence of this process, the resistance measured during this heating curve is higher in the vicinity of T_R compared to a curve acquired without a prior ramp-reversal process. Upon heating into the fully metallic state, the resistance-increase is erased and the original R vs. T curve is recovered.

A heuristic model was suggested for the RRM, based on three properties that are commonly observed in temperature-driven first order phase-transitions of correlated oxide thin films:

i. The transition occurs through phase-coexistence in which two spatially separated phases coexist, referred to as "spatial phase separation". [13,14] Examples include charge order insulating and ferromagnetic metallic phases in manganites, [15,16] metallic and insulating phases in $NdNiO_3$, [17,18] VO_2, [11] V_2O_3 [12] and others. [19]

ii. The different electronic phases in these systems also have different lattice structures, i.e., the electronic transition is coupled to a structural transition. [9,10,20,21].

iii. Strain changes the properties of the transition. [22] Specifically, it can change the critical temperature. [23–26]

The RRM model postulates that the boundaries between co-existing phases have a significant role in the memory effect. [8] Since different lattice structures are coupled to each phase, then along phase boundaries of co-existing phases, the lattice will be distorted. If the distortion is stabilized during the ramp reversal process, the newly formed local strains, referred to as 'scars', will change the local transition temperature. [22,23,27,28] Recent optical measurements provided direct evidence to the existence of phase boundary scars. [29] This heuristic model qualitatively captures the central features previously reported for the RRM:

1. A memory is erased upon heating above the T_R in which it was created, and all memory is erased following heating into the metallic state.
2. Additional memories can be written without erasing existing ones and are maintained over a long period of time.
3. The resistance increase in the vicinity of T_R is correlated with the temperature coefficient of resistance (TCR = $\frac{1}{R} \cdot \frac{dR}{dT}$) of the material.

In order to broaden our understanding and develop a theoretical account of the RRM, it is important to provide a quantitative measurement of the magnitude of the RRM effect, which is currently missing.

We report here the study of V_2O_3 thin films, chosen since they possess all the essential ingredients to exhibit RRM: 1) a first order temperature driven IMT (at ~150K with a resistance change of ~4 orders of magnitude and a hysteresis of 10K), [9,30] 2) an IMT coupled to a structural phase transition (corundum to monoclinic), [20] 3) a transition showing spatial phase separation [12] and 4) correlation between strain and transition temperature. [30–32]

As anticipated, these properties produce the appearance of the RRM in V_2O_3, showing the generality of the effect. A useful quantitative analysis of the RRM can be introduced by studying the effective temperature shift that the RRM generates, instead of a resistance increase at each temperature. This method removes the strong RRM dependence on the TCR and provides a measure of the averaged increase in T_C induced by the scars. An analysis of the RRM measured at different reversal temperatures and as a function of number of reversal loops provides a quantitative understanding of the effect. The results are well reproduced by a model with only two assumptions: 1) the IMT follows a nucleation-and-growth process [33–35] and 2) the scars induce a local T_c increase. This indicates that scars drive the RRM and the number, or length, of scars dictates the magnitude of the memory effect.

RESULTS

The RRM in V_2O_3 is demonstrated using a protocol of sequential R vs. T measurements, as shown in Figure 1 for a 50nm epitaxial V_2O_3 thin film on an r-cut sapphire substrate (see 'Methods' for details). Major loops (ML) are obtained from a heating and cooling R vs. T with minimum and maximum temperatures outside the hysteretic region of the sample, i.e., reaching a single-phase state. In a reversal loop (RL), the heating ramp begins at the low temperature of the ML, and is reversed at the “reversal temperature”, T_R (within the phase-coexistence region). The RRM protocol, shown in Figures 1a (R vs. T) and 1b (heating-and-cooling protocol), begins with a number of MLs that overlap (red lines, measured between 100K to 200K, only the last is shown in Figure 1b), indicating that the R vs. T measurements are reproducible and stable. This is

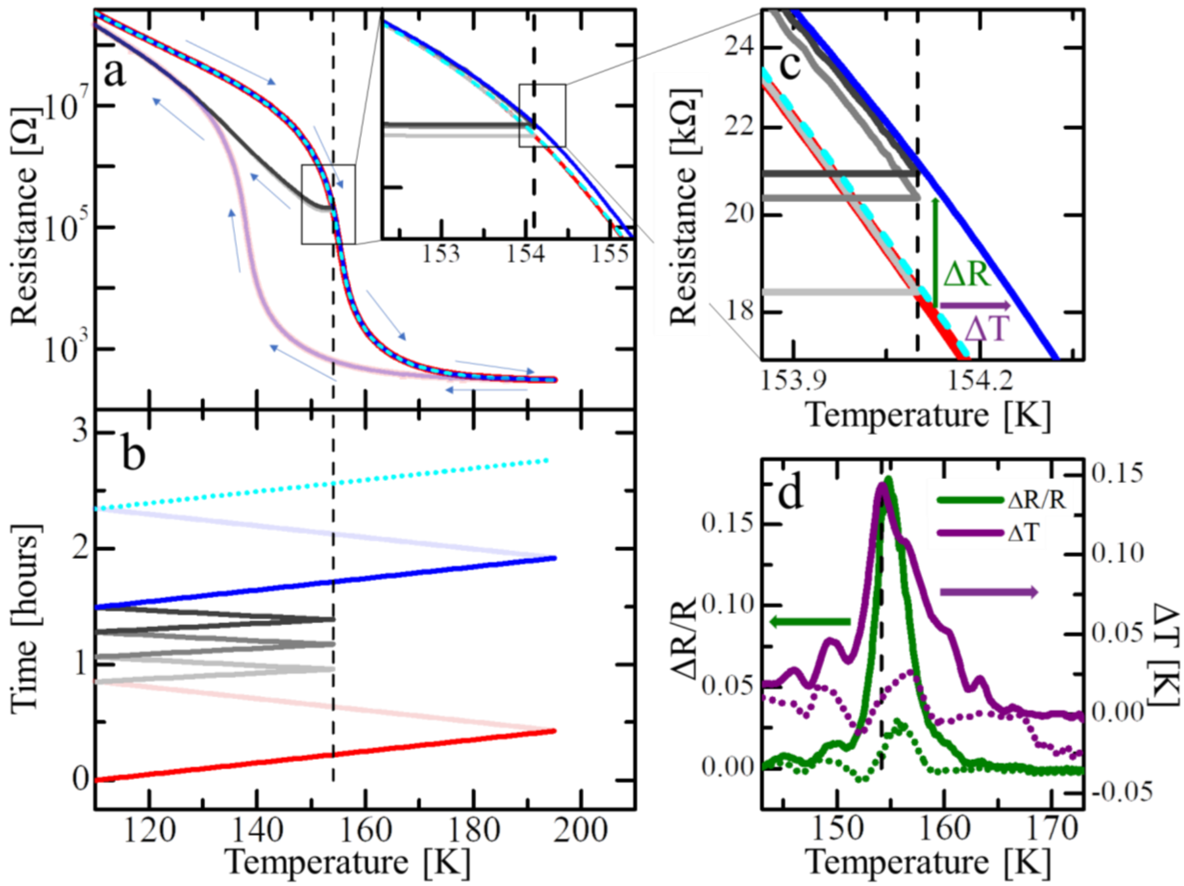

Figure 1. Ramp-reversal in V_2O_3. (a) Color coded R vs. T of full ramp-reversal sequence and (b) the corresponding Time (y-axis) vs Temperature (x-axis). Color coding: red – first ML; graded grey to black – RLs; blue – ML following the three RLs; dashed cyan – another ML (only heating). Perpendicular black line marks T_R = 154.1, in all panes. Inset is zoom-in on T_R region. (c) Additional zoom-in of the T_R region. Arrows mark ΔR and ΔT. d) Plots of ΔR/R (green, left axis) and ΔT (purple, right axis) vs T after the RLs (solid lines), showing RRM peak; and after the following ML measurement (dotted lines) showing that the memory was erased.

followed by three successive RLs with T_R = 154.1 K, plotted as increasingly darker grey lines. T_R is plotted as a perpendicular dashed line, for reference. Each subsequent loop develops a rise in resistance close to T_R relative to the previous, see Figure 1c for a zoom-in around T_R. The next heating ML, plotted in blue, shows a relative increase in resistance with a maximum in the vicinity of T_R, best observed in the inset of Figure 1a. The final heating ML measurement, dashed cyan line, best seen in Figure 1c, recovers the initial R vs. T, demonstrating erasure of the RRM by heating above T_R.

Figure 1c presents two possible analyses of the RRM signal, with the red curve being the virgin ML and the blue the ML right after the RLs. For each temperature one can extract either an increase in resistance, ΔR (green arrow), or the temperature shift needed for the virgin resistance to reach the RRM induced resistance, ΔT (purple arrow). Figure 1d presents the relative change in resistance – $\Delta R/R$ (used previously for RRM analysis), and the effective temperature shift – ΔT, as a function of temperature (solid lines, color coding in figure description). Both plots show an increase in the vicinity of T_R (T_R is marked by the black perpendicular dashed line). We plot and discuss the ΔR vs. T analysis below. The erasure of the memory, due to heating above T_R, is evidenced in the analysis of the following ML (dotted curves, same color coding), where the peaks vanish. In V_2O_3, as demonstrated previously for VO_2 and $NdNiO_3$, RRM memories written at different reversal temperatures can exist concurrently when written in a specific order, [8] see Supplemental Material Figure S2 [36]. We note in passing that there is no memory effect when performing the ramp reversal on the cooling branch, see SM Figure S3 [36]. This is similar to what was previously shown [8] in VO_2 and $NdNiO_3$.

Figure 2 shows a comparison of different analyses of the RRM signal, ΔR (Figure 2a), $\Delta R/R$ (Figure 2b) and ΔT (Figure 2c). We present similar analysis for VO_2 in SM Figure S4 [36].

The RRM was measured following ten RL cycles and at three different reversal temperatures, at the beginning (blue, T_R=148.3 K), center (red, T_R=154.3 K) and end (green, T_R=162.3) of the IMT. The vertical dashed lines mark the three reversal temperatures. The TCR (Figure 2b, black line and right axis) is plotted for comparison.

The three curves in the ΔR analysis, Figure 2a, show large fluctuations at low temperatures and peaks correlated with their reversal temperatures (T_Rs are marked by grey dashed lines). The peak of the high T_R measurement, green curve, is rather small (a few Ohms), it can be observed only in the zoom, inset of Figure 2a. The amplitude of the reversal-temperature peak is proportional to the amplitude of the resistance at that temperature. Thus, for the red and green curves the peak is much smaller than the measurement fluctuations, which are nominally larger in the insulating phase.

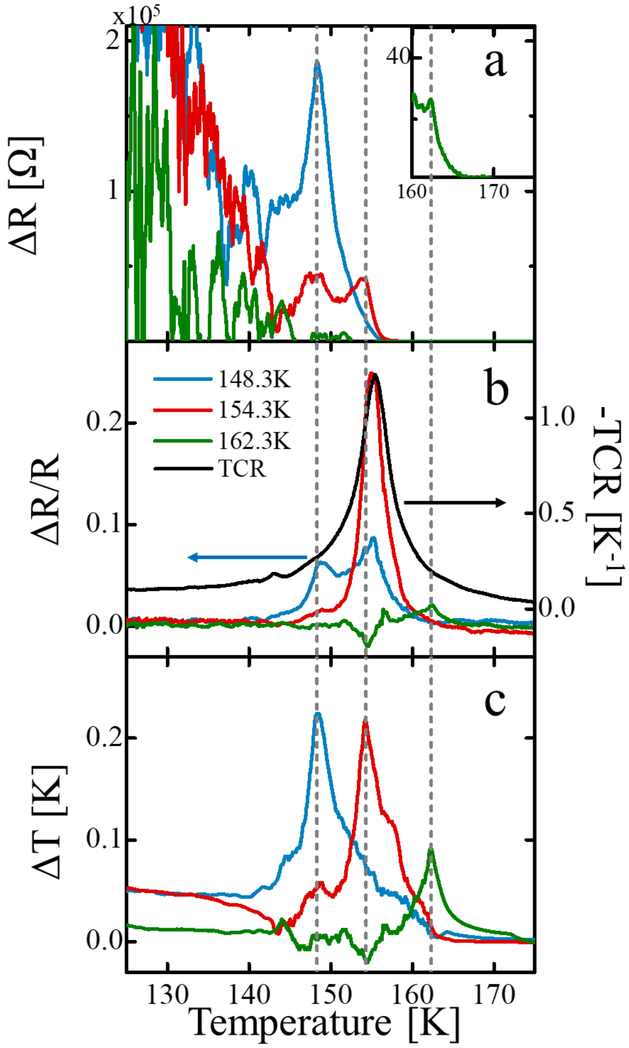

Figure 2. Comparing RRM analyses methods for three different reversal temperatures. a) ΔR vs T, b) ΔR/R vs. T and c) ΔT vs. T. The three reversal temperatures (with ten RLs) are: 148.5K (blue), 154.5K (red) and 162.6K (green), corresponding to the beginning, middle and end of phase transition, respectively. T_R values marked by perpendicular grey dashed lines. The inset in (a) is a zoom-in for T_R = 162.6K. The TCR is plotted in black in (b), right axis.

The ΔR/R analysis, Figure 2b, removes this resistance dependence. The ΔR/R curves also show peaks correlating with their reversal temperature. The low-temperature fluctuations are now suppressed, but the curves have additional features beside the peaks, e.g., there is a second maximum in the blue curve and a minimum in the green curve. The T_R-related ΔR/R peaks' amplitude no longer scale with the resistance (at T_R), they now follow the magnitude of the TCR at the reversal temperature. [8] Note that the additional features are most pronounced where the TCR is large. Additionally, the ΔR/R maximum shifts slightly away from T_R and toward the TCR maximum, best seen in the red curve in Figure 2b, and for VO_2 in SM Figure S4 [36]. The ΔT analysis is presented in Figure 2c. The maximum signal for all three curves occurs at the corresponding T_R, and their amplitude is not related to the TCR. The curves of ΔT may appear wider in some cases (compared to ΔR/R). There is some noise in the curves, but these additional features are smaller than the T_R-related peaks. A comparison of the ΔT and ΔR/R analyses of different materials (V_2O_3, thick and thin VO_2 and $NdNiO_3$) is presented in SM section S5 [36]. The ΔT amplitude is found to be of similar scale in all materials, while ΔR/R is dominated by the different TCRs and therefore prohibits comparison. The comparison between different analyses is further addressed in the discussion.

An analysis of the ΔT signal as a function of the number of reversal loops at different T_Rs is presented in Figure 3. Similar measurements for VO_2 thin films are shown in SM section S6 [36]. Figures 3a and 3b show the change in ΔT for increasing number of RLs, one through twenty (color coding appears in figure), for T_R near the beginning (148 K, Figure 3a) and the end (164 K, Figure 3b) of the IMT. ΔT is larger at the beginning of the IMT compared to the end. In both cases, there is a substantial increase in ΔT between one and three loops, but the increase is less pronounced with additional RLs, especially when T_R is near the IMT end. To follow the evolution of ΔT, we plot in Figure 3c the maximum ΔT, ΔT_{MAX}, as a function of number of RLs. Note that at the beginning of the IMT (red) the RRM magnitude continues to increase with loop number, whereas

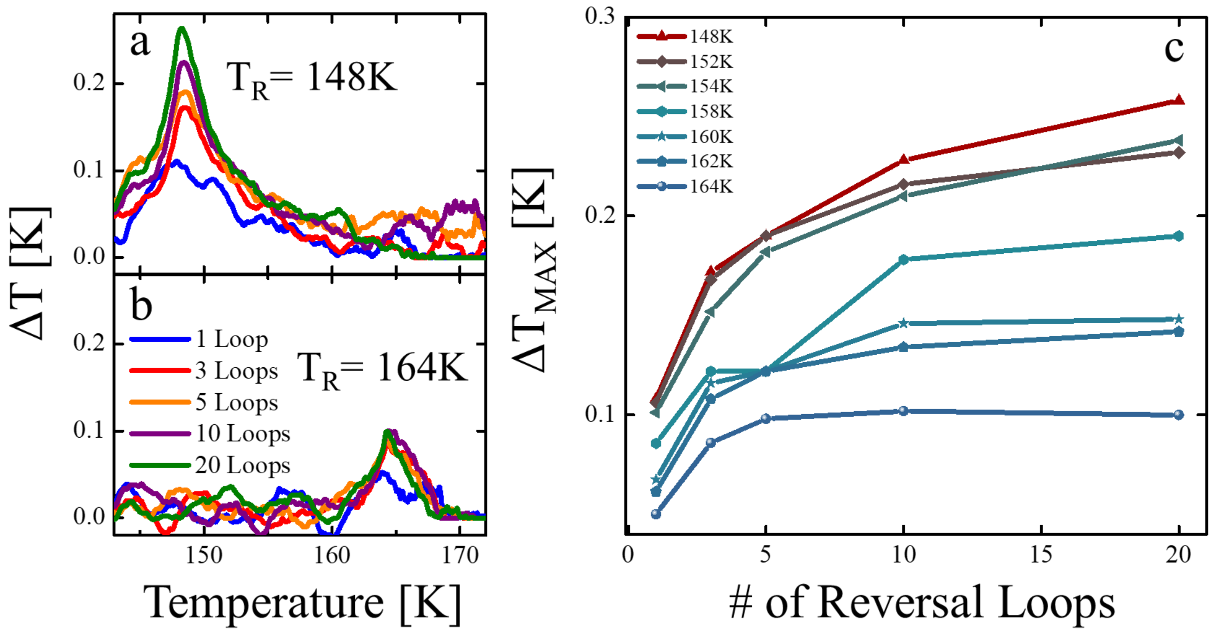

Figure 3. Ramp-reversal analysis for different temperatures and number of RLs. a, b) ΔT vs. T at two reversal temperatures (a) 148K and (b)164K, for different numbers of RLs from one to twenty. Color coding appears in b). c) Maximum value of ΔT peak (ΔT_{MAX}) as function of number of RLs for temperatures along the transition. Color coding of temperature appears in figure.

towards the end of the IMT (blue) the effect is smaller and saturates faster with number of RLs. We discuss these features in detail below.

DISCUSSION

The hypothesized model for the origin of RRM is based on "scars" developing at the coexisting metal-insulator phase boundaries as the temperature ramp-reversal is performed. [8] These scars modify the local T_C (plausible, due to local strain changes [25,30–32]). In the case presented herein, the scars modify the unperturbed R vs. T curve by delaying the growth of metallic domains during the next heating process, i.e., increasing the local T_C. This delay appears as a relative resistance increase. When the system is heated sufficiently above T_R, the scars are "healed", and the memory is erased. Ideally, an analysis of the RRM signal (Figure 1d, Figure 2 and SM Figure S2 [36]) should reflect the effects of the scars and their increase of local T_C. The ΔR magnitude is proportional to the film resistance at each temperature. The normalized ΔR, $\Delta R/R$, correlates with the TCR – which is the rate of resistance change during the IMT. Thus, they do not portray solely the effect of scars and the properties of the RRM. However, the ΔT analysis can naturally capture the scars' contribution to local changes of T_C. Note that the measured effect of local increases in T_C by the microscopic scars on the macroscopically measured ΔT may be complex. This is analogous in nature to effects that local changes in resistance may have on macroscopic resistance measurements. [37] Having more regions with local increases in T_C or having a larger increase in T_C – will both lead to measurements of a larger ΔT. Thus, different models corresponding to any theoretical scenario can now be developed and tested by comparing to the ΔT analysis. In general, such models must consider that the resistance measured is of a percolation network. Note that ΔT is not exactly $\Delta R/R$ normalized to the TCR, see SM section S8 [36] for details.

The effects of the T_R and number of RLs on the magnitude of the RRM can be analyzed in the framework of the scar-model. V_2O_3 and VO_2 transition through nucleation-and-growth of metallic domains in the insulator phase during heating (or insulating domains in the metallic phase during cooling). [33–35] The metallic domains nucleate at random positions (with possible correlations) during the IMT. [12,33,38] The nucleated domains continue to grow during heating, while new metallic domains nucleate within the remaining insulating phase. We model the contribution of scars and the percolative IMT on the RRM signal as follows (see SM section S7 [36] for a detailed description): 1) We assume that metallic domains nucleate at random points during the heating cycle and grow with temperature. 2) During the temperature ramp-reversal, scars are formed at each metal-insulator phase-boundaries, which remain when the sample is cooled. 3) In the next loop, again, nucleation occurs randomly, and metallic domains grow when heated. 4) The growth of the new domains are hindered by the scars (created in previous RLs).

Within this model, the free parameters are the temperature dependent probability for nucleation of sites, and the temperature dependent growth of these sites. We assume that the nucleation of sites follows a Gaussian distribution with the center T_{avg}, when the metallic fraction is 0.5, σ_T, chosen as half the transition width, and N, the total number of nucleations (nucleation density). We also assume that the nucleated regions grow linearly with temperature in all directions, therefore growing quadratically, $R_{site}=A\cdot dT$. R is the site radius, dT is the change in temperature from nucleation, and A is a scaling parameter. The parameters N (nucleation density) and A were refined to emulate the metallic fraction extracted from the experimental R vs. T measurements as shown in Figure 4a. The simulated transition (purple) reproduces well the experimental metallic fraction (green line), that was extracted using the effective medium approximation. [34,39] Thus, there are no free parameters for the scar simulation. Further details of the model can be found in the S7. [36] Figure 5b shows the normalized total scar length (boundaries of nucleated sites) for different T_R and for different number of consecutive RLs. The correlation between experimental ΔT (Figure 3c) and simulated scars' length (Figure 4b), indicates a linear relation between the two. The simulation reproduces the experimental ΔT for the entire T_R range and the number of RLs, except for some deviation at the lowest reversal temperatures, where the metallic fraction also deviates (see Figure 4a).

The behavior of ΔT is well accounted for by scar-creation at phase boundaries. Figure 4c shows the simulated scars created for low (148K) and high (164K) reversal temperatures and after

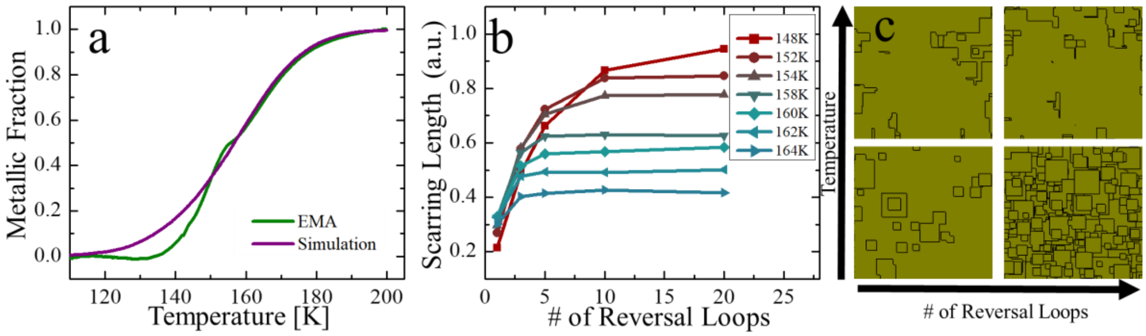

Figure 4. a) Plot of metallic fraction vs. temperature extracted from the effective medium approximation (EMA) compared to the simulation using the fitting parameters (see SI section S6). b) Normalized length of scars ("Scarring Length") at different T_R along the IMT as a function of number of reversal loops. c) Spatial image of simulated scars (black lines) created at different temperatures (148K and 164K) and for different number of RLs (two and forty).

few (two) or many (forty) RLs. At low temperatures, near the beginning of the IMT, the metallic domains are small and therefore leave more space for the creation of new scars in subsequent loops through new nucleation sites. This leads to an increase in the total length of scars vs. number of RLs, and requires more RLs to saturate. This is shown in the bottom panels of Figure 4c. At high temperatures, near the end of the IMT (see top panels of Figure 4c), the metallic domains are larger and leave less space for the creation of new scars with each loop. As a result, the system reaches a saturated state after a few RLs. Our results also indicate that the scars must be much smaller than the domains they surround, indicating that they are of sub-micron scale. Additionally, there is no indication that the increase in local T_C from the scars changes with reversal temperature.

We note that the scar-model of the RRM is able to well-explain the measurements reported herein and previous results. However, it is a heuristic model and as such, is not material specific and cannot provide quantitative, system specific predictions. For this, a first principle theoretical model that is dependent on explicit material properties is required.

In summary, we report the existence of the RRM effect in V_2O_3 thin films that were known to have properties crucial for the memory effect, corroborating the generality of the RRM. We present an analysis of ΔT, which provides a measure of the effective local T_C increase induced by the scars appearing at the phase boundaries. Using this methodology and numerical simulations, we study the evolution of RRM with number of RLs at different reversal temperatures across the IMT. We demonstrate that the changes in RRM magnitude correlates well with the length of scars formed during the ramp-reversal. These results imply that scar formation and healing provide the mechanism for the RRM, and local sub-micron strains in the scars are a plausible driving force. Our findings support a general mechanism behind the RRM, suggesting it should appear in any system exhibiting a first-order metal-insulator transition coupled to a structural phase transition.

METHODS

Film Deposition: Growth of 50 nm V_2O_3 thin films was performed at a substrate temperature of 700°C by RF magnetron sputtering in 8 mTorr of ultra-pure Ar using a home-made V_2O_3 target. After sputtering, the samples were promptly removed from the substrate heater and rapidly cooled at an initial a rate of ~90 K/min. More details and structural analysis of the films can be found in ref. [30]

Details and characteristics for VO_2 samples can be found in the SM section S1 [36] Ref. [40] and previous work. [8,36] Electrodes for transport measurements were wire bonded directly to the films.

Transport Measurements: Measurements were acquired in three different measurement systems: commercial QD- PPMS, commercial Janis closed cycle refrigerator and home- made insert, all showing similar results. R vs. T was performed in a four- probe geometry. A constant current source (with voltage compliance of 10V) was used to avoid excess Joule heating when the transition to the metallic phase began. The R vs. T measurements were performed while continuously sweeping the temperature at 3K/min. A range of ramp rates from 0.5-10 K/min were tested to confirm reliability of temperature sensor and correlation of sample temperature to sensor temperature, to ensure accuracy and reproducibility. There were only slight changes in the magnitude of the measured ramp reversals. The usage of 3K/min was to optimize measurement time and accuracy (noise). Comparison of the different ramp rates are shown in SM section S9. [36]

ASSOCIATED CONTENT

The following files are available free of charge.

Supplemental Material including 9 sections and 9 figures, PDF

AUTHOR INFORMATION

Corresponding Author

Amos Sharoni – Department of Physics and Institute of Nanotechnology and Advanced Materials, Bar Ilan University 5290002, Ramat Gan Israel

Authors

Elihu Anouchi – Department of Physics and Institute of Nanotechnology and Advanced Materials, Bar Ilan University 5290002, Ramat Gan Israel

Yoav Kalcheim – Department of Physics, University of California San Diego, La Jolla, CA 92093, USA

Department of Materials Science and Engineering, Technion, Israel Institute of Technology, Haifa, 3200003, Israel

Ivan K. Schuller - Department of Physics, University of California San Diego, La Jolla, CA 92093, USA

Present Addresses

†If an author's address is different than the one given in the affiliation line, this information may be included here.

Funding Sources

The research at BIU was supported by the ISRAEL SCIENCE FOUNDATION (grant No. 569/16). YK acknowledges funding from the Norman Seiden Fellowship for Nanotechnology and Optoelectronics and the ISRAEL SCIENCE FOUNDATION (grant No. 1031/21). The research at UCSD was supported by the Air Force Office of Scientific Research under award number FA9550-20-1-0242.

Notes

The experiments were conceived jointly, the data was extensively debated, and the paper was written by multiple iteration between all the coauthors.

ACKNOWLEDGMENT

ABBREVIATIONS

RRM, Ramp Reversal Memory

TCR, Temperature Coefficient of Resistance

IMT, Insulator Metal Transition

R vs. T, Resistance vs Temperature

RL, Reversal Loop

T_R, Reversal Temperature

ML, Major Loops

EMA, Effective Medium Approximation

REFERENCES

[1] E. Dagotto, M. Brehm, B.-G. Chae, P.-C. Ho, G. O. Andreev, B.-J. Kim, S. J. Yun, A. V. Balatsky, M. B. Maple, F. Keilmann, et al., *Complexity in Strongly Correlated Electronic Systems.*, Science **309**, 257 (2005).

[2] J. H. Ngai, F. J. Walker, and C. H. Ahn, *Correlated Oxide Physics and Electronics*, Annu. Rev. Mater. Res. **44**, 1 (2014).

[3] S. N. Dorogovtsev, A. V. Goltsev, and J. F. F. Mendes, *Critical Phenomena in Complex Networks*, Rev. Mod. Phys. **80**, 1275 (2008).

[4] E. Morosan, D. Natelson, A. H. Nevidomskyy, and Q. Si, *Strongly Correlated Materials*, Adv. Mater. **24**, 4896 (2012).

[5] H. Kuwahara, Y. Tomioka, Y. Moritomo, A. Asamitsu, M. Kasai, R. Kumai, and Y. Tokura, *Striction-Coupled Magnetoresistance in Perovskite-Type Manganese Oxides*, Science **272**, 80 (1996).

[6] J. G. Bednorz and K. A. Mueller, *Perovskite-Type Oxides - the New Approach to High-Tc Superconductivity*, Rev. Mod. Phys. **60**, 585 (1988).

[7] J. Wang, J. B. Neaton, H. Zheng, V. Nagarajan, S. B. Ogale, B. Liu, D. Viehland, V.

Vaithyanathan, D. G. Schlom, U. V. Waghmare, et al., *Epitaxial $BiFeO_3$ Multiferroic Thin Film Heterostructures*, Science **299**, 1719 (2003).

[8] N. Vardi, E. Anouchi, T. Yamin, S. Middey, M. Kareev, J. Chakhalian, Y. Dubi, and A. Sharoni, *Ramp-Reversal Memory and Phase-Boundary Scarring in Transition Metal Oxides*, Adv. Mater. **29**, 1605029 (2017).

[9] F. J. Morin, *Oxides Which Show a Metal-to-Insulator Transition at the Neel Temperature*, Phys. Rev. Lett. **3**, 34 (1959).

[10] J. B. Torrance, P. Lacorre, A. I. Nazzal, E. J. Ansaldo, and C. Niedermayer, *Systematic Study of Insulator-Metal Transitions in Perovskites $RNiO_3$ (R =Pr, Nd, Sm, Eu) Due to Closing of Charge-Transfer Gap*, Phys. Rev. B **45**, 8209 (1992).

[11] M. M. Qazilbash, M. Brehm, B.-G. Chae, P.-C. Ho, G. O. Andreev, B.-J. Kim, S. J. Yun, A. V Balatsky, M. B. Maple, F. Keilmann, et al., *Mott Transition in VO_2 Revealed by Infrared Spectroscopy and Nano-Imaging.*, Science **318**, 1750 (2007).

[12] A. S. McLeod, E. van Heumen, J. G. Ramirez, S. Wang, T. Saerbeck, S. Guenon, M. Goldflam, L. Anderegg, P. Kelly, A. Mueller, et al., *Nanotextured Phase Coexistence in the Correlated Insulator V_2O_3*, Nat. Phys. **13**, 80 (2016).

[13] G. Allodi, R. De Renzi, F. Licci, and M. W. Pieper, *First Order Nucleation of Charge Ordered Domains in $La_{0.5}Ca_{0.5}MnO_3$ Detected by ^{139}La and ^{55}Mn NMR*, Phys. Rev. Lett. **81**, 4736 (1998).

[14] M. Imada, A. Fujimori, and Y. Tokura, *Metal-Insulator Transitions*, Rev. Mod. Phys. **70**, 1039 (1998).

[15] M. Fäth, S. Freisem, A. A. Menovsky, Y. Tomioka, J. Aarts, and J. A. Mydosh, *Spatially Inhomogeneous Metal-Insulator Transition in Doped Manganites*, Science **285**, 1540 (1999).

[16] K. H. Ahn, T. Lookman, and A. R. Bishop, *Strain-Induced Metal-Insulator Phase Coexistence in Perovskite Manganites*, Nature **428**, 401 (2004).

[17] G. Mattoni, P. Zubko, F. Maccherozzi, A. J. H. van der Torren, D. B. Boltje, M. Hadjimichael, N. Manca, S. Catalano, M. Gibert, Y. Liu, et al., *Striped Nanoscale Phase Separation at the Metal–Insulator Transition of Heteroepitaxial Nickelates*, Nat. Commun. **7**, 13141 (2016).

[18] K. W. Post, A. S. McLeod, M. Hepting, M. Bluschke, Y. Wang, G. Cristiani, G. Logvenov, A. Charnukha, G. X. Ni, P. Radhakrishnan, et al., *Coexisting First- and Second-Order Electronic Phase Transitions in a Correlated Oxide*, Nat. Phys. **14**, 1056 (2018).

[19] C. Beekman, W. Siemons, T. Z. Ward, M. Chi, J. Howe, M. D. Biegalski, N. Balke, P. Maksymovych, A. K. Farrar, J. B. Romero, et al., *Phase Transitions, Phase Coexistence, and Piezoelectric Switching Behavior in Highly Strained $BiFeO_3$ Films*, Adv. Mater. **25**, 5561 (2013).

[20] P. D. Dernier and M. Marezio, *Crystal Structure of the Low-Temperature Antiferromagnetic Phase of V_2O_3*, Phys. Rev. B **2**, 3771 (1970).

[21] A. J. Millis, *Lattice Effects in Magnetoresistive Manganese Perovskites*, Nature **392**, 147 (1998).

[22] N. B. Aetukuri, A. X. Gray, M. Drouard, M. Cossale, L. Gao, A. H. Reid, R. Kukreja, H.

Ohldag, C. A. Jenkins, E. Arenholz, et al., *Control of the Metal–Insulator Transition in Vanadium Dioxide by Modifying Orbital Occupancy*, Nat. Phys. **9**, 661 (2013).

[23] T. Yamin, S. Wissberg, H. Cohen, G. Cohen-Taguri, and A. Sharoni, *Ultrathin Films of VO_2 on r-Cut Sapphire Achieved by Postdeposition Etching*, ACS Appl. Mater. Interfaces **8**, 14863 (2016).

[24] N. F. Quackenbush, H. Paik, M. J. Wahila, S. Sallis, M. E. Holtz, X. Huang, A. Ganose, B. J. Morgan, D. O. Scanlon, Y. Gu, et al., *Stability of the M2 Phase of Vanadium Dioxide Induced by Coherent Epitaxial Strain*, Phys. Rev. B **94**, 085105 (2016).

[25] J. H. Park, J. M. Coy, T. Serkan Kasirga, C. Huang, Z. Fei, S. Hunter, and D. H. Cobden, *Measurement of a Solid-State Triple Point at the Metal-Insulator Transition in VO_2*, Nature **500**, 431 (2013).

[26] D. G. Schlom, L. Q. Chen, C. B. Eom, K. M. Rabe, S. K. Streiffer, and J. M. Triscone, *Strain Tuning of Ferroelectric Thin Films*, Annu. Rev. Mater. Res. **37**, 589 (2007).

[27] Y. Kalcheim, N. Butakov, N. M. Vargas, M. H. Lee, J. Del Valle, J. Trastoy, P. Salev, J. Schuller, and I. K. Schuller, *Robust Coupling between Structural and Electronic Transitions in a Mott Material*, Phys. Rev. Lett. **122**, 057601 (2019).

[28] P. Salev, J. Del Valle, Y. Kalcheim, and I. K. Schuller, *Giant Nonvolatile Resistive Switching in a Mott Oxide and Ferroelectric Hybrid*, Proc. Natl. Acad. Sci. U. S. A. **116**, 8798 (2019).

[29] A. Zimmers, S. Basak, F. Simmons, P. Salev, I. Schuller, L. Aigouy, and E. Carlson, *Spatial Mapping of Ramp Reversal Memory in VO_2*, in *APS March Meeting 2022* (2022).

[30] N. Alyabyeva, J. Sakai, M. Bavencoffe, J. Wolfman, P. Limelette, H. Funakubo, and A. Ruyter, *Metal-Insulator Transition in V_2O_3 Thin Film Caused by Tip-Induced Strain*, Appl. Phys. Lett. **113**, 9131 (2018).

[31] D. B. McWhan, A. Menth, J. P. Remeika, W. F. Brinkman, and T. M. Rice, *Metal-Insulator Transitions in Pure and Doped V_2O_3*, Phys. Rev. B **7**, 1920 (1973).

[32] Y. Kalcheim, C. Adda, P. Salev, M. Lee, N. Ghazikhanian, N. M. Vargas, J. del Valle, and I. K. Schuller, *Structural Manipulation of Phase Transitions by Self- Induced Strain in Geometrically Confined Thin Films*, Adv. Funct. Mater. **30**, 2005939 (2020).

[33] A. Sharoni, J. G. Ramírez, and I. K. Schuller, *Multiple Avalanches across the Metal-Insulator Transition of Vanadium Oxide Nanoscaled Junctions*, Phys. Rev. Lett. **101**, 026404 (2008).

[34] T. Yamin, Y. M. Strelniker, and A. Sharoni, *High Resolution Hall Measurements across the VO_2 Metal-Insulator Transition Reveal Impact of Spatial Phase Separation*, Sci. Rep. **6**, 19496 (2016).

[35] E. Abreu, S. Wang, J. G. Ramírez, M. Liu, J. Zhang, K. Geng, I. K. Schuller, and R. D. Averitt, *Dynamic Conductivity Scaling in Photoexcited V_2O_3 Thin Films*, Phys. Rev. B **92**, 85130 (2015).

[36] See Supplemental Material at for details of film fabrication, more RRM properties in V_2O_3, similar analyses in VO_2, different material comparison and Scar Model explanation.

[37] Y. Frenkel, N. Haham, Y. Shperber, C. Bell, Y. Xie, Z. Chen, Y. Hikita, H. Y. Hwang, E. K. H. Salje, and B. Kalisky, *Imaging and Tuning Polarity at SrTiO3 Domain Walls*, Nat.

Mater. **16**, 1203 (2017).

[38] S. Liu, B. Phillabaum, E. W. Carlson, K. A. Dahmen, N. S. Vidhyadhiraja, M. M. Qazilbash, and D. N. Basov, *Random Field Driven Spatial Complexity at the Mott Transition in* VO_2, Phys. Rev. Lett. **116**, (2016).

[39] D. Bergman and Y. Strelniker, *Magnetotransport in Conducting Composite Films with a Disordered Columnar Microstructure and an In-Plane Magnetic Field*, Phys. Rev. B **60**, 13016 (1999).

[40] J. Trastoy, Y. Kalcheim, J. del Valle, I. Valmianski, and I. K. Schuller, *Enhanced Metal–Insulator Transition in* V_2O_3 *by Thermal Quenching after Growth*, J. Mater. Sci. **53**, 9131 (2018).